

Inductive magnetosphere–ionosphere coupling

W. Lotko*

Thayer School of Engineering, Dartmouth College, Hanover, NH 03755-8000, USA

Received 24 February 2004; received in revised form 30 March 2004; accepted 30 March 2004

Abstract

Inductive coupling of a global magnetospheric model to a global ionospheric–thermospheric model is described. Existing schemes based on electrostatic coupling are valid for magnetospheric variability occurring on time scales of order 100 s or longer. The formulation developed here extends the validity of the coupling model to time scales of order 10 s, while retaining the physics of quasi-static coupling as the long time-scale limit. Both lumped and distributed formulations for the coupling region are derived. The induction gives rise to magnetic and ion kinetic energy storage at low altitude. The induced ion polarization current on average causes an upward magnetic body force on the plasma which may facilitate massive outflow.

© 2004 Elsevier Ltd. All rights reserved.

Keywords: Interaction between ionosphere and magnetosphere; Electric fields in the magnetosphere; Electric fields in the ionosphere

1. Introduction

From the perspective of large-scale numerical modeling of geospace, magnetosphere–ionosphere (MI) coupling describes the physical interaction between the collisionless plasma of a global magnetospheric model (GM) and the neutral and ionized gases of a global ionospheric–thermospheric model (GIT). This coupling introduces feedback and scale-interactivity in the form of Maxwell shear stresses and time-variable mass and energy fluxes at the boundaries of the two models. The “MI coupling region” as illustrated in Fig. 1 may be regarded as the spatial domain between the low-altitude boundary of the GM model (located above the Alfvén speed maximum near 1–2 R_E altitude) and the high-altitude boundary of the GIT model (located above the F2 peak).

Treatment of the MI coupling region as a distinct spatial region is necessary for several reasons. The speed of propagation of ultralow frequency electromagnetic signals traversing the MI coupling region (the Alfvén speed) can approach the speed of light in large-scale auroral plasma cavities (Persoon et al., 1988). The implied constraints on numerical stability of an MHD code make extension of a GIT or GM model into this region impractical for realistic conditions. In effect, transmission, reflection and absorption of electromagnetic power flowing into and out of the region (Lysak and Dum, 1983; Vogt and Haerendel, 1998; Streltsov and Lotko, 2003; Keiling et al., 2003) occur almost instantaneously on the numerical cadence of a global simulation.

The formation of parallel electric fields in the MI coupling region, and the myriad non-MHD plasma processes that accompany parallel electric fields (Paschmann et al., 2003), are not easily incorporated into a large-scale MHD model. A simple parameterization of the processes that produce field-aligned electron beams

*Tel.: +1-603-646-3485; fax: +1-603-646-3856.

E-mail address: william.lotko@dartmouth.edu (W. Lotko).

URL: <http://www.dartmouth.edu/~wlotko>.

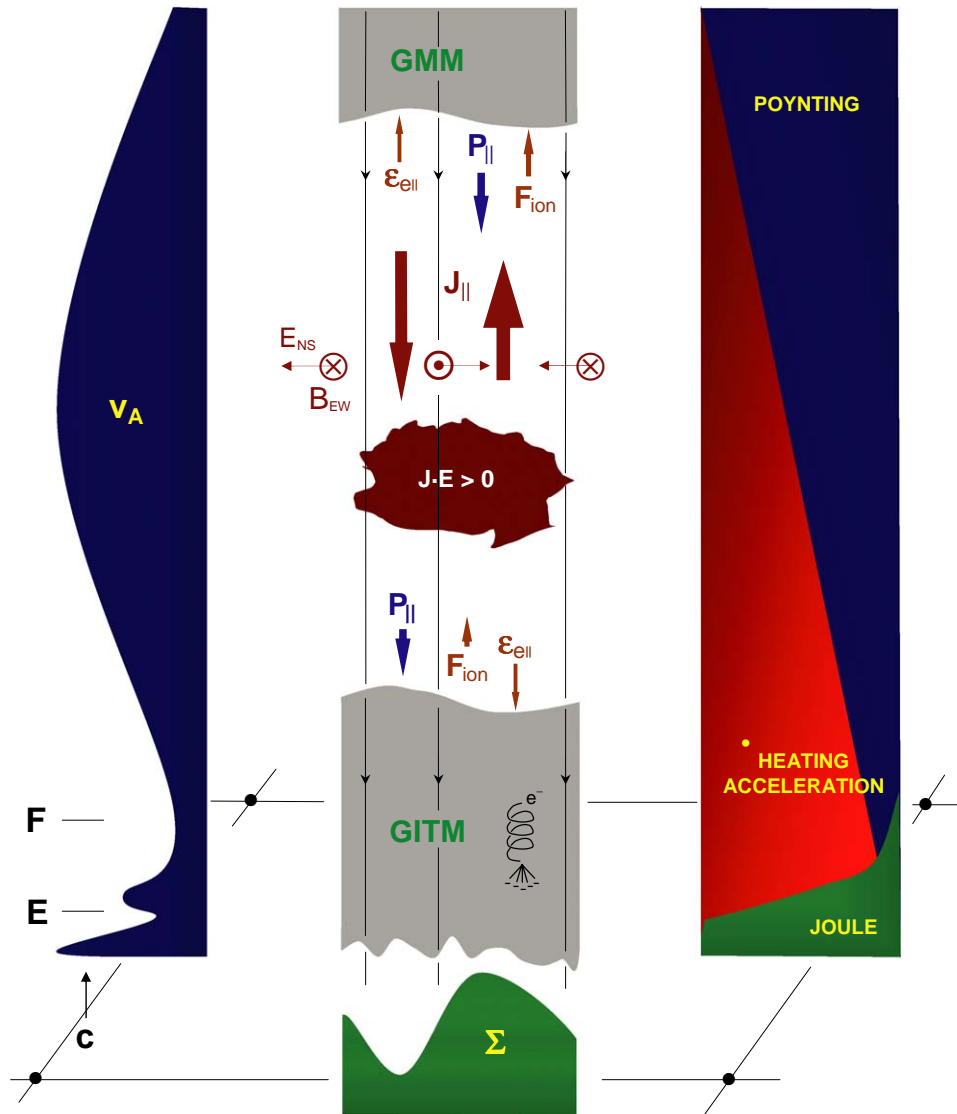


Fig. 1. Illustration of a 2D section of a dissipative MI coupling region located between a GM model and a GIT model. The configuration of upward and downward field-aligned currents J_{\parallel} , with associated north–south electric fields E_{NS} and east–west magnetic fields B_{EW} , Poynting flux P_{\parallel} and electron energy fluxes $\epsilon_{e\parallel}$ in the coupling region resemble in situ satellite measurements reported by Lotko et al. (1998). Poynting flux flows into the region through the high-altitude boundary and is partially absorbed before entering the ionosphere at the low-altitude boundary. Upward accelerated electrons in the downward current region carry energy flux into the GM domain and deplete the conductivity Σ in the GIT domain. Downward accelerated electrons in the upward current region carry energy flux into the GIT domain and enhance the ionization and conductivity of the ionosphere. Ion upflows F_{ion} enter the MI coupling region from the GIT domain and leave the region through the GMM boundary after being further energized in the coupling region. The Alfvén speed profile in the E- and F-regions and in the MI coupling region is illustrated on the left, with the speed of light c indicated at the bottom. The altitudes where electromagnetic energy transmission (Poynting), collisionless acceleration and heating, and collisional Joule dissipation prevail are indicated on the right.

(Lyons, 1992; Carlson et al., 1998; Chaston et al., 2003; Cattell et al., 2004) and the energy flux they carry into the ionosphere–thermosphere and magnetosphere is needed.

Lastly, the collisionless physics of ion acceleration and heating in the MI coupling region is a subgrid

phenomenon in large-scale models. For this reason, ionospheric upwelling (Moore et al., 1999), the development of a transonic polar wind (Banks and Holzer, 1969; Yau et al., 1984), and the outflow of auroral and polar cusp ions (Collin et al., 1998; McFadden et al., 1998; Tung et al., 2001) are probably best modeled in the

form of flux sources at the boundaries of large-scale models.

The current generation of MI coupling models employed in global simulations all treat the MI coupling region as an integrated electrostatic circuit element. The auroral and polar distribution of ionospheric electric potential is calculated from the familiar 2D elliptic equation (Vasyliunas, 1970) based on current continuity, Ohm's law, and the scalar potential representation for the ionospheric electric field. The conductivity in the Ohm's law is determined either by an empirical formula in standalone GM models (Fedder et al., 1995; Raeder, 2003) or by ion production and transport in the GIT component of a coupled magnetosphere–ionosphere–thermosphere (CMIT) model (Raeder et al., 2001; Ridley et al., 2003; Wang et al., 2004; Wiltberger et al., 2004). The LFM and Raeder coupling modules also include an active element in the conductivity that depends on variable electron precipitation. The mono-energy of the precipitating electrons in these modules is derived from the linearized Knight (1973) formula relating the field-aligned potential drop to the upward field-aligned current. Electron precipitation modifies the Joule heating rate and the thermodynamics of the thermosphere and ionosphere in the CMIT models of Raeder et al. (2001) and Wang et al. (2004).

The existing MI coupling models are also lumped models, in the sense that they specify the fields and electron flux only at the boundaries of the coupling region rather than the distributions of the fields and transport processes within the coupling region. Although a lumped approach is computationally efficient, it limits the physics that can be treated.

In this paper, the electrostatic approach to coupling a GM model to a GIT model is extended to include effects of magnetic induction. Distributed and lumped formulations are derived. Dynamic MI coupling including induction generally entails Alfvén wave dynamics (e.g. Paschmann et al., 2003, Chapter 3 and references therein). However, when the time scales of interest are much greater than the propagation time of an Alfvén wave through the coupling region ($\int d\ell/v_A(\ell) \sim 1$ s), phase delays associated with incident and reflected waves may be ignored. This limit is the basis for electrostatic models of MI coupling. The analysis of Sections 2 and 3 shows that the large Alfvén speed limit also facilitates a simple yet accurate formulation of inductive MI coupling in the global simulation gap at low altitudes, including the effects of Alfvén waves and weak magnetic compression on the perpendicular spatial scales currently resolvable by global models and on time scales for which electrostatic coupling ceases to be valid. The approximations enabling this formulation are validated quantitatively by numerical simulations of standing Alfvén waves at auroral latitudes (e.g. Rankin et al., 2000) and qualitatively by satellite observations in

the coupling region (Nagatsuma et al., 1996). This simple analytical representation of low-altitude electro-dynamics and its use in coupling a GM model to a GIT model evidently has been overlooked until now.

The importance of magnetic induction in MI coupling is threefold. First, as shown in Section 3, it introduces an imaginary part in the effective impedance of the coupling region. For magnetospheric variability occurring on time scales less than about 100 s, the magnitude of the imaginary part of the impedance is greater than the real part (essentially the inverse of the height-integrated ionospheric conductivity). The resulting phase shift between the electric and magnetic fields (Knudsen et al., 1992; Nagatsuma et al., 1996) produces an inductive electric field at the low-altitude boundary of the GM model that can be very different from its electrostatic counterpart. The magnetic flux through the low-altitude boundary of the GM model is also modified. This inductive phase shift may correct some of the (\sim few) minute timing errors in auroral-electrojet forecasts derived from GMI simulations (Wiltberger et al., 2003). Second, induction enables storage of magnetic and ion sloshing energy, which modifies the flow of electromagnetic power through the region. When coupled back into the plasma dynamics of the coupling region, this energy reservoir may provide a conduit for the production of plasma beams and heat. Third, ion polarization currents accompany magnetic induction. The resulting $\mathbf{J}_\perp \times \mathbf{B}_\perp$ body force on the ions on average propels them upward along the ambient magnetic field (Allan, 1992), which may facilitate massive outflows.

The field-aligned potential drop across a resistive-inductive coupling region depends on the effective impedance of the medium, the current flowing through it, and the explicit time variation in the current. As a consequence, the formulation of a current–voltage relation to parameterize the energy of precipitating electrons is more complicated when magnetic induction enters the dynamics. Nevertheless, it is shown in Section 4 that the energy of accelerated electrons produced by an inductive parallel electric field may be calculated approximately as the product of the field-aligned current density and the “lumped resistance” of the coupling region. Challenges and approaches for the development of more general models of electron parallel energization, leading to both downgoing and upgoing electron energy fluxes, are discussed. Consideration of the Poynting theorem in Section 5 provides insights into the inductive power flow through the MI coupling region. The inductive model for MI coupling is summarized as an algorithm in Section 6.

The development begins in the next section with a general analysis of the equations of motion of the ionized species. The objective of this preliminary analysis is to identify the conditions of validity of the inductive model for MI coupling, Eqs. (8)–(11), on

which the remainder of the paper is based. The resulting model is asymptotic in the small parameter $\varepsilon \equiv 1/\Sigma_P \mu_0 v_A$, where v_A is the Alfvén speed at the top of the GIT model and Σ_P is the height-integrated Pedersen conductivity.

2. Inductive response at low altitude

The momentum equation for charged species s , including pressure, gravitational, electric and Lorentz forces, and drag resulting from collisions between charged species and between neutral and charged species, is given by

$$m_s n_s \frac{D_s \mathbf{v}_s}{Dt} = -\nabla \cdot \mathbf{P}_s - m_s n_s \mathbf{G}(r) + e_s n_s [\mathbf{E} + \mathbf{v}_s \times (\mathbf{B} + \mathbf{B}_0)] - \sum_k m_s n_s v_{sk} (\mathbf{v}_s - \mathbf{v}_k), \quad (1)$$

with $D_s/Dt = \partial/\partial t + \mathbf{v}_s \cdot \nabla$.

Magnetic perturbations \mathbf{B} in the low- β plasmas of the ionosphere and the low-altitude magnetosphere are observed to be much smaller in magnitude ($\sim 10^{-3}$) than the geomagnetic field \mathbf{B}_0 . We therefore neglect their effect in the Lorentz force in Eq. (1). Defining $\mathbf{b}_0 = \mathbf{B}_0/B_0$, and taking the vector product of \mathbf{b}_0/B_0 with Eq. (1), then gives

$$\mathbf{v}_{\perp s} = \frac{\mathbf{E} \times \mathbf{b}_0}{B_0} + \frac{\mathbf{b}_0}{e_s n_s B_0} \times \left[m_s n_s \frac{D_s \mathbf{v}_s}{Dt} + \nabla \cdot \mathbf{P}_s + m_s n_s \mathbf{G}(r) + \sum_k m_s n_s v_{sk} (\mathbf{v}_s - \mathbf{v}_k) \right]. \quad (2)$$

Above the F2 peak in the mid-to-high latitude ionosphere and low-altitude magnetosphere, the electric drift \mathbf{v}_E represented by the first term on the right is much greater than the terms in the square bracket (e.g. p. 370 Schunk and Nagy, 2000). This disparity allows the substitution $\mathbf{v}_{\perp s} = \mathbf{v}_E$ on the right-hand side of Eq. (2):

$$e_s n_s (\mathbf{v}_{\perp s} - \mathbf{v}_E) = \frac{m_s n_s}{B_0^2} \frac{d\mathbf{E}_{\perp}}{dt} + \frac{\mathbf{b}_0}{B_0} \times \left[\nabla \cdot \mathbf{P}_s + m_s n_s \mathbf{G}(r) + \sum_n m_s n_s v_{sn} (\mathbf{v}_E - \mathbf{v}_n) \right]. \quad (3)$$

\mathbf{E}_{\perp} is the perpendicular electric field in the plasma, and

$$\frac{d\mathbf{E}_{\perp}}{dt} = \frac{\partial \mathbf{E}_{\perp}}{\partial t} + \mathbf{b}_0 \times [(\mathbf{v}_E + \mathbf{v}_{\parallel}) \cdot \nabla \mathbf{v}_E] \simeq \frac{\partial \mathbf{E}_{\perp}}{\partial t} + (\mathbf{v}_E + \mathbf{v}_{\parallel}) \cdot \nabla \mathbf{E}_{\perp}. \quad (4)$$

The low-frequency, electric current density \mathbf{j}_{\perp} flowing perpendicular to the ambient magnetic field above the F2 peak of the ionosphere is obtained by summing Eq. (3) over all charged species:

$$\mathbf{j}_{\perp} = \frac{\rho}{B_0^2} \frac{d\mathbf{E}_{\perp}}{dt} + \frac{\mathbf{b}_0}{B_0} \times \left[\nabla \cdot \mathbf{P} + \rho \mathbf{G}(r) + \sum_{s,n} m_s n_s v_{sn} (\mathbf{v}_E - \mathbf{v}_n) \right]. \quad (5)$$

The mass density $\rho = \sum m_s n_s$. The pressure tensor $\mathbf{P} = \sum \mathbf{P}_s$ is summed over ion species and electrons. The last term in Eq. (5) involves summation \sum_n over neutral species and \sum_s over charged species.

When the variables in Eq. (5) are scaled to a characteristic velocity v_c , magnetic perturbation B_c , electric field $v_c B_c$, mass density ρ_c , pressure P_c , collision frequency ν_c , time scale τ_c and length scale $v_c \tau_c$, the resulting equation is found to contain four non-dimensional groups. Each group is the coefficient of one of the terms on the right-hand side of the resulting non-dimensional form of Eq. (5). In order of appearance from left-to-right, the coefficients are:

$$\varepsilon = \frac{v_c^2}{v_A^2}, \quad \varepsilon_P = \varepsilon \frac{B_0}{B_c} \frac{c_s^2}{v_c^2}, \quad \varepsilon_G = \varepsilon \frac{B_0}{B_c} \frac{G \tau_c}{v_c} \quad \text{and} \quad \varepsilon_c = \varepsilon \nu_c \tau_c. \quad (6)$$

These non-dimensional parameters are all small in the ionosphere and low-altitude magnetosphere, primarily because $v_c/v_A \ll 1$ (cf. Section 3.3 below and numerical estimates in Tables 1 and 2). In the limit, $\varepsilon \rightarrow 0$, we have $\mathbf{j}_{\perp} = 0$, or equivalently $\nabla \cdot \mathbf{j}_{\parallel} \mathbf{b}_0 = 0$ implying $j_{\parallel}/B_0 = \text{constant}$. The inductive model derived in the following sections is based on this limit.

Ampere's law relates the perpendicular current density to the magnetic perturbation:

$$\mu_0 \mathbf{j}_{\perp} = \nabla_{\parallel} \times \mathbf{B}_{\perp} + \nabla_{\perp} \times \mathbf{B}_{\parallel} \simeq 0. \quad (7)$$

The compressional perturbation \mathbf{B}_{\parallel} in the coupling region has two sources. One is the rotational Hall current in the ionosphere, which induces a compressional surface wave with amplitude decreasing exponentially above the E-layer (Yoshikawa, 2002). The e-folding length is 100 km when the horizontal wavelength of the imposed electric field or field-aligned current is $2\pi \times 100$ km. The coupling model developed below is valid in this perpendicular length-scale regime (see Section 3.2). In this case, the ionospherically induced magnetic compression is confined to the lower ionosphere and does not extend into the coupling region. The second source of \mathbf{B}_{\parallel} is direct induction by rotational polarization currents flowing within the coupling region. The resulting $O(\varepsilon)$ compression in the magnetic field derived from Eq. (10) below remains finite at the

Table 1
Characteristic parameters at three altitudes in the coupling region

Physical variable	Characteristic value	Numerical estimate (altitude in km)		
		500	1000	10,000
Velocity \mathbf{V}_\perp^a (10^3 km/s)	v_c	1	1	6
Magnetic field \mathbf{B}_\perp^b (nT)	B_c	100	90	27
Electric field \mathbf{E}_\perp (mV/m)	$v_c B_c$	100	100	1
Current density \mathbf{J}_\perp (nA/m ²)	$B_c/\mu_0 v_c \tau_c$	8	7	0.4
Plasma density n (10^{10} m ⁻³)	n_c	1–5	1	0.001
Collision frequency ν_{sn} (s ⁻¹)	v_c	0.1	—	—
Pressure P (nPa)	P_c	1.5	0.5	0.01
Time t (s)	τ_c	10	10	10
Length ℓ (10^3 km)	$v_c \tau_c$	10	40	500
Dipole field \mathbf{B}_0 (10^3 nT)	B_0	90	70	6
Mass density ρ^c (10^{-19} (kg/m ³))	ρ_c	10,000	2700	0.17
Alfvén speed v_A (10^3 km/s)	$B_0/(\mu_0 \rho_c)^{1/2}$	2.5	3.8	41
Ion sound speed c_s (km/s)	$(P_c/\rho_c)^{1/2}$	1.2	1.4	24
Background temperature T (eV)	P_c/n_c	0.2	0.5	10

^aCharacteristic speed from Section 3.3 is $v_c = |(\mu_0 \Sigma_P)^{-1} - i\omega \Delta \ell|$.

^bWave magnetic field assumed to decrease with altitude as $r^{-3/2}$. See Eq. (14).

^c $\rho_c = n_c m_i$ where $m_i = m_{O^+}$ at 500-, 1000-km altitude and m_{H^+} at 10,000-km altitude.

Table 2
Non-dimensional parameters at three altitudes in the coupling region

Parameter	Dimensionless group	Numerical estimate ^a (altitude in km)		
		500	1000	10,000
ε	$(v_c/v_A)^2$	0.16	0.07	0.02
$\varepsilon_P \times 1000$	$\varepsilon (B_0/B_c)(c_s/v_c)^2$	0.21	0.11	0.08
$\varepsilon_G \times 1000$	$\varepsilon (B_0/B_c)(G\tau_c/v_c)$	16	6.8	0.35
ε_C	$\varepsilon(v_c \tau_c)$	0.16	—	—

^aEstimated from values in Table 1.

high-altitude boundary of the coupling region and ensures $\nabla \cdot \mathbf{B} = 0$ throughout the coupling region.

Given these considerations, Ampere’s law in the limit $\varepsilon \rightarrow 0$ becomes

$$\nabla_{\parallel} \times \mathbf{B}_\perp = 0, \tag{8a}$$

$$\nabla_\perp \times \mathbf{B}_\perp = \mu_0 \mathbf{j}_{\parallel}. \tag{8b}$$

The perturbed magnetic field derived from Eq. (8a) is used in Faraday’s law to determine the electric field:

$$(\nabla \times \mathbf{E})_\perp = \nabla_{\parallel} \times \mathbf{E}_\perp + \nabla_\perp \times \mathbf{E}_{\parallel} = -\frac{\partial \mathbf{B}_\perp}{\partial t}. \tag{9}$$

Eq. (9) must be supplemented by a constitutive relation between \mathbf{E}_{\parallel} and \mathbf{j}_{\parallel} . Ohm’s law is used for this relation in Section 4. The primary distinction between the inductive model for MI coupling developed in the next sections and the electrostatic model used by the LFM and

Raeder GM models is the retention of finite $\partial \mathbf{B}_\perp / \partial t$ on the right-hand side of Eq. (9). Magnetic induction also gives rise to magnetic compression and the polarization current given below.

The first-order \mathbf{B}_{\parallel} and \mathbf{j}_\perp may be calculated from the zeroth-order \mathbf{E}_\perp derived from Eq. (9)

$$\frac{\partial \mathbf{B}_{\parallel}}{\partial t} = -\nabla_\perp \times \mathbf{E}_\perp, \tag{10}$$

$$\mathbf{j}_\perp = \frac{\rho}{B_0^2} \frac{d\mathbf{E}_\perp}{dt}. \tag{11}$$

Eqs. (8)–(11), together with appropriate boundary conditions, describe the inductive response of the mid- to high-latitude ionosphere and low-altitude magnetosphere (below a few R_E) to low-frequency, electromagnetic disturbances originating in the magnetosphere. Eq. (11) for the polarization current

additionally requires a model for the ion parallel momentum and mass density, which brings the ion parallel dynamics of the coupling region into consideration. This development will not be pursued here other than to note that the solutions derived below couple into but do not explicitly depend on the ion mass continuity, parallel momentum and energy equations.

3. Zero parallel electric field

3.1. Solution along dipole fieldlines

At low altitude, the geomagnetic field is dipolar to a good approximation. The high- and low-altitude boundary conditions on the MI coupling region are imposed on spherical surfaces, which are not normal to the dipole field. The non-orthogonal, boundary-constrained flux coordinates of Proehl et al. (2002) prescribe a general approach to the differential geometry for this problem. Because this geometry is only weakly non-orthogonal in the mid-to-high latitude domain of interest here, we will develop solutions to the differential equations (8a) and (9) in the simpler orthogonal dipole coordinates ϕ , v and ℓ defined in the appendix. When $E_{\parallel} = 0$, we obtain

$$\frac{1}{h_{\phi}} \nabla_{\ell}(h_{\phi} B_{\phi}) = 0, \quad \frac{1}{h_v} \nabla_{\ell}(h_v B_v) = 0, \quad (12)$$

$$\frac{1}{h_{\phi}} \nabla_{\ell}(h_{\phi} E_{\phi}) = -\frac{\partial B_v}{\partial t}, \quad \frac{1}{h_v} \nabla_{\ell}(h_v E_v) = \frac{\partial B_{\phi}}{\partial t}. \quad (13)$$

The first two equations provide the following representation for \mathbf{B}_{\perp} , valid along each field line:

$$B_{\phi} = B_{\phi m}(\phi, v, t) \frac{h_{\phi m}}{h_{\phi}}, \quad (14a)$$

$$B_v = B_{v m}(\phi, v, t) \frac{h_{v m}}{h_v}. \quad (14b)$$

$B_{\phi m}$ and $B_{v m}$ are boundary values of B_{ϕ} and B_v on the surface $r = r_m$, where h_{ϕ} and h_v assume the values $h_{\phi m}$ and $h_{v m}$. These boundary values can be obtained from the time-dependent solution of the GM model (e.g., the LFM model) by choosing the surface $r = r_m$ to be the low-altitude boundary of the magnetospheric model.

We now use Eq. (14) in Eq. (13) and integrate the resulting equations along field lines to obtain

$$E_{\phi} = E_{\phi i}(\phi, v, t) \frac{h_{\phi i}}{h_{\phi}} - \alpha_{\phi}(\ell) \frac{h_{v m}}{h_{\phi}} \frac{\partial B_{v m}}{\partial t}, \quad (15a)$$

$$E_v = E_{v i}(\phi, v, t) \frac{h_{v i}}{h_v} + \alpha_v(\ell) \frac{h_{\phi m}}{h_v} \frac{\partial B_{\phi m}}{\partial t}. \quad (15b)$$

The geometric factors $\alpha_{\phi, v}(\ell)$ are given in the appendix. $E_{\phi i}$ and $E_{v i}$ are boundary values specified at the top of the ionospheric model, $r = r_i$, which we choose as the

reference point $\ell = 0$ in the southern hemisphere and $\ell = \ell_L$ in the northern hemisphere, i.e., the L-shell-dependent fieldline length is ℓ_L . In the coupled magnetosphere–ionosphere–thermosphere model described by Wang et al. (2004) and Wiltberger et al. (2004), the top of the ionosphere is located at $r_i = 1 R_E + 500$ km.

Evaluation of Eq. (15) at the upper boundary of the coupling region ($r = r_m$), or its generalization derived in Section 4 below, provides the boundary condition for Faraday’s law required by the LFM solver. This inductive electric field solution and the associated magnetic flux correction implied by Eq. (10) may be used to resolve an inconsistency that arises in the LFM solution near the low-latitude boundary when a purely electrostatic boundary condition is imposed (Lyon et al., 2004).

3.2. Determination of $\mathbf{E}_{\perp i}$

The required boundary condition on $\mathbf{E}_{\perp i}$ is provided by current continuity in the ionosphere combined with Ohm’s law, $\mathbf{j}_{\perp i} = \underline{\sigma} \cdot (\mathbf{E}_{\perp i} + \mathbf{u}_n \times \mathbf{B}_0)$, integrated from the bottom of the ionosphere up to the height $r = r_i$:

$$\nabla_{\perp} \cdot \underline{\Sigma} \cdot \mathbf{E}_{\perp i} = j_{\parallel i} \sin \delta - \nabla_{\perp} \cdot \underline{\Sigma} \cdot (\mathbf{u}_n \times \mathbf{B}_0). \quad (16)$$

$j_{\parallel i}$ is the field-aligned current at $r = r_i$, calculated from Ampere’s law (8b) using the mapped magnetic perturbation $\mathbf{B}_{\perp i}$ determined by Eq. (14). The geometric factor $\sin \delta \equiv \hat{\mathbf{r}} \cdot \mathbf{b}_0 = 2 \cos \theta (1 + 3 \cos^2 \theta)^{-1/2}$ arises from the fact that the magnetic field intersects the ionosphere at an oblique angle relative to the height-integrated (radial) direction (Wolf, 1973). The “magnetic dip angle” δ is essentially constant over the height of the ionosphere in the thin spherical shell model. Note that $\sin \delta \simeq 0.9$ at $\theta = 45^\circ$, so the dip-angle correction is relatively small in the low-altitude region at mid and high latitudes.

The large parallel conductivity of the ionosphere implies that the fieldlines are essentially equipotentials, allowing $\mathbf{E}_{\perp i}$ to be treated as constant with respect to the height integration. The neutral wind velocity \mathbf{u}_n in Eq. (16) is also taken to be (a) independent of altitude and (b) the same for the different neutral species. If the dependence of \mathbf{u}_n with altitude is known, its effect in Eq. (16) can be more accurately modeled by height-integrating the product, $\underline{\sigma} \cdot \mathbf{u}_n \times \mathbf{B}_0$, rather than the conductivity alone. The collisionality of the lower ionosphere maintains a more or less common velocity for the different neutral species.

The conductance tensor is given by

$$\underline{\Sigma} = \frac{1}{\sin \delta} \begin{pmatrix} \Sigma_P / \sin \delta & \Sigma_H \\ -\Sigma_H & \Sigma_P \sin \delta \end{pmatrix} \quad (17)$$

where Σ_P and Σ_H are the height-integrated Pedersen and Hall conductivities (e.g. Schunk and Nagy, 2000).

In imposing the ionospheric boundary condition Eq. (16), we will assume that ionospheric induction can be neglected and that the electric field at the ionosphere can be represented in terms of an electrostatic potential:

$$\mathbf{E}_{\perp i} = -\nabla_{\perp} \Phi_i(\phi, v, \ell_i, t). \quad (18)$$

Neglect of the inductive response of the ionosphere is valid when the characteristic frequency ω and perpendicular wavenumber k_{\perp} of variations in the field-aligned current satisfy $\omega L_{\text{eff}}/R_{\text{eff}} \ll 1$ where $L_{\text{eff}} = \mu_0/k_{\perp}(1 + \coth k_{\perp}d)$ is the effective inductance of the ionosphere and $R_{\text{eff}} \simeq \Sigma_P/(\Sigma_P^2 + \Sigma_H^2)$ is the resistance of the ionosphere (Yoshikawa, 2002), i.e. the time variation is slow in comparison with the L – R time constant of the ionosphere. The inductance depends on the height $d \approx 100$ km of the E layer above the (presumed) perfectly conducting earth. This condition implies

$$\frac{\mu_0 \Sigma_P f \lambda}{1 + \coth k_{\perp}d} \left(1 + \frac{\Sigma_H^2}{\Sigma_P^2} \right) \ll 1. \quad (19)$$

where $f = 2\pi/\omega$ and $\lambda = 2\pi/k_{\perp}$. The inequality is satisfied, for example, when $f = 0.1$ Hz and $\lambda = 100$ km, with an ionosphere characterized by $\Sigma_P = 5$ S and $\Sigma_H = 10$ S. Treatment of higher conductivity states and/or larger scale current systems varying on 10-s time scales will require development of a fully inductive ionosphere rather than the electrostatic ionospheric model implemented here and in all existing GIT models.

3.3. Characteristic impedance

To check the self-consistency of the assumptions leading to the above solution ($\varepsilon \ll 1$), it is instructive to consider the special case of constant conductance and constant neutral wind velocity for a two-dimensional configuration with no variation in the coordinate ϕ . The solution to the Poisson equation obtained from (16)–(18) for a low-latitude boundary condition where both the convection electric field and field-aligned current are zero is

$$(\mu_0 \Sigma_P / \sin^3 \delta) E_{vi} = B_{\phi i}. \quad (20)$$

With Eqs. (3.1) and (20) in Eq. (3.1), and setting $\partial/\partial t = -i\omega$, we find for the characteristic velocity

$$v_c = \frac{E_v}{B_{\phi}} = \left[\frac{\sin^3 \delta}{\mu_0 \Sigma_P} \frac{h_{vi}}{h_{\phi i}} - i\omega \alpha_{\phi}(\ell) \right] \frac{h_{\phi}}{h_v} \approx \frac{1}{\mu_0 \Sigma_P} - i\omega \Delta \ell. \quad (21)$$

High-latitude approximations for $\sin \delta$, h_{ϕ}/h_v and $\alpha_{\phi}(\ell)$ (see appendix) have been implemented in the last form of Eq. (21). $\Delta \ell$ is the field-aligned distance measured from the top of the ionospheric model ($r = r_i$). The

characteristic impedance Z_c of the medium is defined as

$$Z_c \equiv \mu_0 v_c \approx \frac{1}{\Sigma_P} - i\mu_0 \omega \Delta \ell. \quad (22)$$

The first and second terms on the right-hand side of Eq. (22), respectively, characterize the electrostatic and inductive response of the medium. The first term is zero for a perfectly conducting ionosphere whereas the second is zero for steady-state conditions. The large Alfvén speed limit has eliminated the inhomogeneity of the medium from the formulation, giving the same small ε expansion of the impedance derived by Knudsen et al. (1992) for a homogeneous medium.

The response at low altitude is essentially electrostatic when $\mu_0 \omega \Delta \ell \ll 1/\Sigma_P$. In this case, the characteristic velocity is $v_c \approx 1/\mu_0 \Sigma_P$. At high latitudes where Σ_P varies from 2 to 20 S, v_c ranges from 4×10^4 to 4×10^5 m/s. In the mid-latitude nightside ionosphere, the Pedersen conductivity may be as low as 0.5 S, where $v_c \approx 10^6$ m/s. In comparison, the Alfvén speed v_A typically exceeds 10^6 m/s at the top of the ionospheric model ($n_{O^+} \approx 10^{10} \text{ m}^{-3}$). From these estimates we conclude that the condition, $\varepsilon \equiv v_c^2/v_A^2 \ll 1$, for validity of the field solutions (14)–(15) is satisfied in the electrostatic limit ($\mu_0 \omega \Delta \ell \ll 1/\Sigma_P$), except possibly in the topside ionosphere under unusual conditions in which a very weak E layer is sustained below a strongly enhanced F layer (cf. numerical estimates in the appendix).

The response at low altitude becomes inductive when $\mu_0 \omega \Delta \ell \gtrsim \Sigma_P^{-1}$. This occurs at relatively high frequency and/or high altitude. For example for frequencies of 1, 10 and 100 mHz, and for $\Sigma_P = 5$ S, the electrostatic and inertial terms in Eq. (22) are equal at field-aligned distances above the ionosphere of $\Delta \ell = 25,000$, 2500 and 250 km, respectively. The low-altitude boundary of the LFM model (and other global MHD models) is typically located at a geocentric distance of 2–3 R_E . The response in the region below this inner boundary therefore becomes substantially inductive when the global model generates field-aligned currents that vary on time scales of order 100 s or less. Note that the condition $v_c^2/v_A^2 \ll 1$ is satisfied above the topside ionosphere, even for strongly inductive conditions, because v_A increases exponentially above the F region.

The numerical eigenvalue solutions reported by Rankin et al. (2000) for a fundamental fieldline resonance at $L = 6$ provide a benchmark for the inductive solutions developed here. They calculated eigenfunctions for both dipole ($f \approx 27$ mHz) and T96 ($f \approx 2$ mHz) magnetic geometry, including a realistic density distribution (from topside $n_{O^+} = 10^{10} \text{ m}^{-3}$ to equatorial $n_{H^+} = 10^6 \text{ m}^{-3}$). The results conform to Eq. (22) with good accuracy from the ionospheric boundary of the calculation, where they chose $\Sigma_P = 10$ S, upward to a fieldline distance nearly halfway to the equator.

4. Finite parallel electric field

4.1. Distributed resistive layer

The results derived above are now generalized to the case when the low-altitude magnetospheric plasma sustains a parallel electric field. Here, we consider parallel electric fields characterized by a microscopic (local) Ohms law:

$$\mathbf{E}_{\parallel} = \eta \mathbf{j}_{\parallel}. \quad (23)$$

The collisionless resistivity η is, in general, a complicated nonlinear and non-local function of the plasma distribution functions and field parameters.

With Eq. (23) in Eq. (9), and separating the resulting vector component equations in dipole coordinates, we obtain

$$\frac{\partial}{\partial \ell} h_{\phi} E_{\phi} = \frac{\partial}{\partial \phi} \eta j_{\ell} - \frac{\partial}{\partial t} h_{\phi} B_v. \quad (24a)$$

$$\frac{\partial}{\partial \ell} h_v E_v = \frac{\partial}{\partial v} \eta j_{\ell} - \frac{\partial}{\partial t} h_v B_{\phi}, \quad (24b)$$

where B_{ϕ} and B_v are given by Eq. (14).

These equations may be integrated following the analysis leading to Eq. (15) and using the fact that $j_{\ell}/B_0 = \text{constant}$ along field lines. Integration from the top of the ionospheric modeling region ($r = r_i$) to an arbitrary field-aligned distance ℓ provides the desired generalization:

$$E_{\phi} = \frac{h_{\phi i}}{h_{\phi}} E_{\phi i}(\phi, v, t) - \alpha_{\phi}(\ell) \frac{h_{vm}}{h_{\phi}} \frac{\partial B_{vm}}{\partial t} + \frac{1}{h_{\phi}} \frac{\partial}{\partial \phi} \mathcal{R} j_{\ell}(\phi, v, \ell, t), \quad (25a)$$

$$E_v = \frac{h_{vi}}{h_v} E_{vi}(\phi, v, t) + \alpha_v(\ell) \frac{h_{\phi m}}{h_v} \frac{\partial B_{\phi m}}{\partial t} + \frac{1}{h_v} \frac{\partial}{\partial v} \mathcal{R} j_{\ell}(\phi, v, \ell, t), \quad (25b)$$

where

$$\mathcal{R} \equiv \frac{1}{B_0} \int_0^{\ell} \eta(\phi, v, \ell', t) B_0(v, \ell', t) d\ell' \quad (26)$$

has the units $\Omega\text{-m}^2$. The system Eq. (25) has now acquired a dissipative element (last term) in addition to the potential (first) and inductive (second) terms.

4.2. Lumped coupling model

A lumped model of the coupling region is useful when the field-aligned distributions of the electric field and magnetic field are not required, but only their perpendicular distributions at the top of the ionosphere designated as $\ell = \ell_i$ and at the inner boundary of the GM model designated as $\ell = \ell_m$ (the field-aligned

coordinates ℓ_i and ℓ_m assume different numerical values in the northern and southern hemisphere, but they map to the same radial distance from the earth in both hemispheres.) The electric field solution at $\ell = \ell_i$ is obtained from the Poisson equation as described in Section 3.2. Evaluation of Eqs. (25)–(26) at $\ell = \ell_m$ provides

$$E_{\phi m} = \frac{h_{\phi i}}{h_{\phi m}} E_{\phi i}(\phi, v, t) - \alpha_{\phi}(\ell) \frac{h_{vm}}{h_{\phi m}} \frac{\partial B_{vm}}{\partial t} + \frac{1}{h_{\phi m}} \frac{\partial}{\partial \phi} \mathcal{R}_m j_{\ell m}(\phi, v, t), \quad (27a)$$

$$E_{vm} = \frac{h_{vi}}{h_{vm}} E_{vi}(\phi, v, t) + \alpha_v(\ell) \frac{h_{\phi m}}{h_{vm}} \frac{\partial B_{\phi m}}{\partial t} + \frac{1}{h_{vm}} \frac{\partial}{\partial v} \mathcal{R}_m j_{\ell m}(\phi, v, t). \quad (27b)$$

Here $j_{\ell m}(\phi, v, t) = j_{\ell}(\phi, v, \ell_m, t)$, and

$$\mathcal{R}_m \equiv \frac{1}{B_{0m}} \int_{\ell_i}^{\ell_m} \eta B_0 d\ell' = \frac{B_{0i}}{B_{0m}} \mathcal{R}_i \quad (28)$$

is a ‘‘lumped resistivity’’ (Lotko, 1986). Note that $\mathcal{R}_m j_{\ell m}(\phi, v, t) = \mathcal{R} j_{\ell i}(\phi, v, t)$ where $j_{\ell i}(\phi, v, t) = j_{\ell}(\phi, v, \ell_i, t)$.

Electrostatic MI coupling follows from the limit ($\partial/\partial t = 0$) of Eq. (27). The parallel potential drop between the magnetospheric and ionospheric boundaries is well defined in the electrostatic limit because the parallel electric field is derivable from an electric potential, $E_{\parallel} = -\nabla_{\parallel} \Phi$. In this case, the integral of Eq. (23) gives

$$\Phi_i - \Phi_m = \mathcal{R}_m j_{\ell m}(\phi, v, t) = \mathcal{R} j_{\ell i}(\phi, v, t). \quad (29)$$

This ‘‘linear’’ current–voltage relation is used in the LFM precipitation model described by Wiltberger et al. (2004) to parameterize the energy of precipitating electrons (also Raeder, 2003). The algorithm takes $j_{\parallel i}$ directly from LFM and calculates the parameterized \mathcal{R}_i using LFM density and pressure variables. $\Phi_i - \Phi_m$ is then calculated from Eq. (29). This algorithm therefore treats the magnetosphere as a constant current source.

When magnetic induction is retained, the effective parallel potential drop depends on the time scale of interest because $E_{\parallel} = -\nabla_{\parallel} \Phi - \partial A_{\parallel} / \partial t$. A_{\parallel} is a magnetic flux function such that $\mathbf{B}_{\perp} = \nabla_{\perp} \times \mathbf{A}_{\parallel}$. However, weak magnetic compressibility ($B_{\parallel} / B_{\perp} \ll 1$) in the coupling region still implies $\nabla_{\perp} \times \mathbf{E}_{\perp} \simeq 0$ to lowest order in the perturbation expansion introduced at the end of Section 2. This distinction between the weakly inductive nature of \mathbf{E}_{\perp} and the fully inductive behavior of \mathbf{E}_{\parallel} is characteristic of shear Alfvén waves.

4.3. Inductive effects on precipitation

The energy of precipitating electrons implicitly influences the solution for \mathbf{E}_\perp because the ionospheric conductivity Σ varies with the state of ionization, which, in turn, is determined either by an empirical conductivity model in a standalone magnetospheric model (Fedder et al., 1995; Raeder, 2003) or via source terms in the ionospheric continuity equation in a coupled magnetosphere–ionosphere–thermosphere model (Raeder et al., 2001; Wang et al., 2004; Wiltberger et al., 2004).

Field-aligned currents carried by the loss cone of adiabatic electrons precipitating through a parallel potential drop obey a lumped Ohm's law of the form given by Eq. (29) (Knight, 1973). In this case, the parameter \mathcal{R}_i is determined by the density and thermal energy of the precipitating electrons (Fridman and Lemaire, 1980). This quasi-static kinetic model for \mathcal{R}_i is valid in the electrostatic limit discussed in Section 3.3. It is the basis for the precipitation module in both the LFM and Raeder GM models.

A current–voltage relation also arises in inductive systems with resistive field-aligned currents carried by a low-energy, thermal distribution of electrons. In particular, the current–voltage relation obtained from the two-fluid simulations reported by Streltsov and Lotko (2003) was found to be parabolic at low current and potential ($\lesssim 5$ kV) with $\Delta\Phi_\parallel \propto j_\parallel^2$ (see also Rönnmark, 2002), and linear at larger potential drops. The potential drop is defined in an inductive system as the net energy acquired by fast electrons (see discussion preceding equation (31) below). The anomalous resistivity model used by Streltsov and Lotko (2003) is a nonlinear function of the field-aligned current density, chosen to model bulk electron parallel drag resulting from current-driven ion-cyclotron turbulence (Lysak and Dum, 1983). The resistive bulk current supports the parallel electric field, while accelerated electrons are produced either by “running away” from the turbulence-entrained bulk or by freely accelerating upon entering the region of parallel electric field from above or below (Pokhotelov et al., 2002). In contrast with the adiabatic kinetic model of Knight, this resistive bulk current model applies to both upward and downward field-aligned currents. FAST satellite observations of electron distributions in turbulent downward current regions indicate that potential drops on the order of a few hundred eV or more are required to sustain the upflowing electron fluxes that carry intense downward field-aligned currents (Carlson et al., 1998; Cattell et al., 2004).

Although the processes leading to field-aligned potential drops differ in detail in upward and downward current regions, the use of a current–voltage relation may be adequate from the perspective of large-scale modeling—provided the value of \mathcal{R}_i is causally adjusted to reflect these differences. Observations in upward

current regions (inverted-V precipitation regions) provide evidence for a lumped resistance $\mathcal{R}_i \sim 10^9 \Omega\text{-m}^2$ (e.g. Lyons et al., 1979; Lu et al., 1991), whereas \mathcal{R}_i is evidently nonlinear and a factor of 4 lower in downward current regions (Temerin and Carlson, 1998; Cattell et al., 2004). Thus, if upward current regions typically require 1 kV of parallel potential drop per $\mu\text{A}/\text{m}^2$ of field-aligned current, then something like 250 V of reverse-biased potential is required per $\mu\text{A}/\text{m}^2$ of downward current.

To implement a current–voltage relation in an inductive system, an effective field-aligned potential drop must be defined. The extension of Eq. (29) to inductive fields is obtained by integrating Eq. (23) directly, without assuming E_\parallel is derivable from a scalar potential:

$$\int_{\ell_i}^{\ell_m} E_\ell d\ell = \mathcal{R}_i J_{\ell i}(\phi, v, t). \quad (30)$$

The integral on the left is the effective potential drop encountered by electrons traversing the MI coupling region with transit time much less than the time scale for variation in E_\parallel . (The speed of a 100-eV electron is about $1R_E/\text{s}$.) When this condition is satisfied, the parallel electric field is essentially static on the electron transit time, and the net energization ε_\parallel per electron can be calculated from

$$\varepsilon_{e\parallel} = e\mathcal{R}_i J_{\parallel i}(\phi, v, t). \quad (31)$$

This relation, when supplemented with a suitable model for \mathcal{R}_i , can be used to specify the precipitating electron energy.

In general, the net energization can be either more or less than $\varepsilon_{e\parallel}$ when the electron transit time across the coupling region is comparable to the time scale for variations in E_\parallel . However, transit-time acceleration is usually associated with inertial Alfvén waves (Chaston et al., 2003; Lysak and Song, 2003), and the transverse scales on which these subgrid kinetic effects prevail cannot be resolved by the current generation of GMI models.

5. Power flow

The system defined by Eqs. (8), (9) and (23) possesses the integral form

$$\begin{aligned} \frac{\partial}{\partial t} \int_V \int \int \frac{B_\perp^2}{2\mu_0} dv &= -\frac{1}{\mu_0} \oint_S \mathbf{E} \times \mathbf{B}_\perp \cdot \hat{n} da \\ &\quad - \int_V \int \int \eta^2_\parallel dv. \end{aligned} \quad (32)$$

To gain some insights into the implications of Eq. (32), we assume the volume integrals in Eq. (32) are bounded

on the top and bottom by magnetic normal surfaces and on the sides by magnetic tangent surfaces on which $\mathbf{E}_{\parallel} = 0$ so that a flux tube representation may be used. With $dv = da d\ell$ and $B_0 da = \text{constant}$, we have

$$\frac{\partial}{\partial t} \int \frac{B_{\perp}^2}{2\mu_0} d\ell = P_{\parallel m} - P_{\parallel i} - \mathcal{R}j_{\parallel i}^2, \quad (33)$$

where

$$P_{\parallel m,i} = \frac{1}{\mu_0} (\mathbf{E}_{\perp} \times \mathbf{B}_{\perp})_{\parallel m,i}, \quad (34)$$

is the component of the Poynting vector parallel to the ambient magnetic field at the magnetospheric (m) and ionospheric (i) boundaries of the coupling region.

Energy conservation requires that $P_{\parallel i}$ be equal to the height-integrated dissipation occurring in the ionosphere–thermosphere–earth region, $r < r_i$. If the GIT model includes only Joule heating, as is the case for the current CMIT models described by Raeder et al. (2001), Wang et al. (2004) and Wiltberger et al. (2004), then $P_{\parallel i}$ must be equal to the Joule dissipation per unit flux tube area in the ionosphere. Making this equivalence explicit and rearranging terms yields

$$P_{\parallel m} = \mathcal{R}j_{\parallel i}^2 + R_C J_{\perp i}^2 + \mathbf{u}_n \cdot \mathbf{J}_{\perp i} \times \mathbf{B}_0 + \frac{\partial}{\partial t} \int_0^{\ell_m} \frac{B_{\perp}^2}{2\mu_0} d\ell, \quad (35)$$

where $\mathbf{J}_{\perp i} = \underline{\Sigma} \cdot (\mathbf{E}_{\perp i} + \mathbf{u}_n \times \mathbf{B}_0)$ is the height-integrated perpendicular current flowing in the ionosphere, and $R_C = \Sigma_P / (\Sigma_P^2 + \Sigma_H^2)$ is the ‘‘Cowling’’ resistance.

Eq. 35 indicates that the electromagnetic energy flux $P_{\parallel m}$ flowing through the lower boundary of the magnetospheric model is dissipated by the development of a parallel electric field (first term on right) with the implied production of field-aligned electron beams and by Joule heating of the ionosphere (second term on right). The work done per unit flux tube area by the ionospheric current on the neutral wind (third term) and the time rate of change of energy per unit flux tube area stored in the magnetic field (last term) may be either positive or negative. Negative work on the neutral wind actually means work done by the neutral wind on the ionospheric plasma ($-\mathbf{u}_n \times \mathbf{B}_0 \cdot \mathbf{J}_{\perp i}$). This usually negligible ‘‘flywheel effect’’ (Lyons et al., 1985) can be important following geomagnetic storms. If enhanced thermospheric stirring by intense stormtime ionospheric currents is followed by a weak convection state, the motoring neutral wind can drag the ionospheric ions with it, thereby producing a motional electric field of magnitude $\mathbf{u}_n \times \mathbf{B}_0$ and a neutral wind-driven perpendicular current $\mathbf{J}_{\perp i}$ carried the collisionally entrained ions.

6. The algorithm

The inductive model for MI coupling derived above may be implemented as follows.

1. At each time step t_k , the GM model provides the magnetic field $\mathbf{B}_{\perp m}(\phi, v, t_k)$ at its inner boundary, corresponding to the upper boundary of the MI coupling region — typically a spherical shell located at 1–2 R_E altitude.
2. This boundary value is used in equations (14) to specify the magnetic field at all altitudes within the coupling region.
3. The field-aligned current in the coupling region is obtained from Ampere’s law (8b). Note that j_{\parallel}/B_0 is constant along field lines in the coupling region.
4. The product of the field-aligned current at the ionospheric boundary and the integral resistivity \mathcal{R}_i (model specified separately) is used in Eq. (31) to determine the ‘‘monoenergy’’ of precipitating electrons. This electron energy is used in the electron precipitation model (specified separately) to evaluate modifications to the ionospheric conductivity $\underline{\Sigma}$ calculated by the GIT model at time step t_k .
5. The field-aligned current at the ionospheric boundary, together with the modified conductivity and neutral wind velocity from the GIT model, are used in the Poisson equation derived from Eqs. (16)–(18) to solve for the electric potential $\Phi_i = \Phi(\phi, v, \ell_i, t_k)$ at the ionospheric boundary of the MI coupling region.
6. The electrostatic potential function $\Phi_m \equiv \Phi(\phi, v, \ell_m, t_k)$ at the inner boundary the GM model is calculated from the formula $\Phi_m = \Phi_i - \mathcal{R}_m j_{\parallel m}$.
7. The electrostatic part of the electric field at the inner boundary of the GM model is calculated as $\mathbf{E}_{\perp \text{static}} = -\nabla_{\perp} \Phi(\phi, v, \ell_m, t_k)$. This portion of the algorithm is the basis for MI coupling in the existing LFM and Raeder GM models.
8. The inductive electric field at the inner boundary of the GM model is calculated as the sum of the inductive part $\mathbf{E}_{\perp \text{inductive}}$, represented by the second term in Eq. (27), and the electrostatic part calculated in step 7. In calculating the inductive term it is necessary to keep two or more time steps (depending on the finite difference scheme for time derivatives) of the magnetic field at the inner boundary of the GM model determined in step 1.
9. The induced parallel component B_{\parallel} of the magnetic field at the inner boundary the GM model is obtained from Eq. (10) by integrating from $t = t_{k-1}$ to t_k . Note that only the inductive part of the electric field from step 8 contributes to \mathbf{B}_{\parallel} . This compressional field when combined with \mathbf{B}_{\perp} from step 2 insures $\nabla \cdot \mathbf{B} = 0$ for all time in the coupling region.

10. The inductive electric field (from step 8) and parallel magnetic field (from step 9) evaluated at the inner boundary of the GM model provide the required boundary conditions on the GM model to calculate the GM solution at time step t_{k+1} (cf. Lyon et al., 2004).
11. Calculation of the distributions of \mathbf{E}_\perp and \mathbf{j}_\perp along field lines in the coupling region requires a distributed model for the resistivity η in Ohm's law (23). Given a model for $\eta(\phi, v, \ell, t)$, the distributed integral resistivity \mathcal{R} is calculated from Eq. (26), which is then used in Eq. (25) to evaluate the \mathbf{E}_\perp everywhere in the coupling region.
12. The perpendicular current everywhere in the coupling region may then be calculated from Eq. (11). However, because \mathbf{j}_\perp in Eq. (11) depends on the distribution of bulk plasma density ρ and parallel velocity v_\parallel (cf. Eq. (4)), evaluation of \mathbf{j}_\perp is not complete without a model for the parallel compressional plasma dynamics of the coupling region, as described by equations of continuity, parallel momentum and energy. The solution for the one-fluid parallel dynamics may be used, for example, to specify a boundary condition on the mass flux through the ITM and GM boundaries. This boundary condition is currently treated in an ad hoc manner in both models.

In the large Alfvén speed limit, the inductive coupling scheme described in steps 1–10 above is self-contained and does not depend on the ion parallel dynamics. However, the ion parallel dynamics of the coupling region does depend on the inductive coupling solution in two ways. First, the convective derivative in the mass continuity, parallel momentum and energy equations depends on the electric drift velocity \mathbf{v}_E derived from the inductive coupling model. Second the parallel momentum equation contains the nonlinear force term $\mathbf{j}_\perp \times \mathbf{B}_\perp$, which, when time-averaged, gives rise to an upward parallel force on the fluid (Allan, 1992).

7. Discussion and summary

Inductive effects begin to modify the electrostatic response of the coupling region when the magnetosphere generates field-aligned currents that vary on time scales less than about 100 s. Induction may become important on even longer time scales for high conductivity states of the ionosphere. For <10-s magnetospheric variability, the high-Alfvén speed approximation on which the analysis of this paper is based begins to break down. When this occurs, the finite propagation time of Alfvén waves through the inhomogeneous coupling region must be considered. These faster dynamics also give rise to an ionospheric induction caused by rotational Hall currents

(Yoshikawa, 2002). This neglected effect influences the reflectivity of the ionosphere and the impedance of the coupling region at frequencies and transverse length scales larger than those treated here.

In contrast with the electrostatic coupling schemes implemented in existing global simulation models, the inductive electric field derived here is accompanied by magnetic compressibility, which dynamically modifies the magnetic flux through the low-altitude boundary of the GM model. Induction also produces a phase shift in the electric field relative to the magnetic field, which is manifested in the complex impedance discussed in Section 3.3. When the inductive (second) term in equations (25) dominates the potential (first) and resistive (third) terms, the boundary condition on Faraday's law required by the GM solver deviates significantly from that given by purely electrostatic coupling.

The complex impedance inferred from measurements of nightside electric and magnetic fields at frequencies of 2–80 mHz and at altitudes of 6000–10,000 km in the auroral-polar cap boundary region (Nagatsuma et al., 1996) agrees qualitatively with the impedance given by Eq. (22). These observations also confirm the expectation that the reflectivity of the ionosphere should increase with frequency (Knudsen et al., 1992), leading to a progressively larger phase shift between electric and magnetic fields with increasing frequency, along with a more oscillatory (up/down) Poynting flux. A transition from quasi-static power flow to inductive power flow is in fact observed at frequencies of about 2.5 mHz, corresponding to transverse length scales on the order of 200 km.

The magnetic energy storage represented by the last term in the energy integral (35) modifies the electromagnetic energy flux flowing through the low-altitude boundary of the GM model, relative to that described by electrostatic coupling (first three terms). The $O(\varepsilon)$ magnetic compressibility derived from Eq. (10) and the ion sloshing motion associated with the $O(\varepsilon)$ polarization current (11) give rise to additional storage terms of the form $(1/2\varepsilon_0) \int \int \int (v_A/c)^2 (dE_\perp^2/dt) dv$ and $(1/2\mu_0) \int \int \int \partial B_\parallel^2/\partial t dv$, respectively. The weak magnetic compression of the coupling region is produced by a Poynting flux $\mathbf{E}_\perp \times \mathbf{B}_\parallel/\mu_0$ through the lateral boundaries. The polarization current imposes a $\mathbf{J}_\perp \times \mathbf{B}_\perp$ body force on the parallel ion motion. On average this force propels ions upward along the ambient magnetic field (Allan, 1992) and, together with transverse ion heating and ionospheric upwelling, may facilitate massive outflows.

The microscopic Ohm's law (23) for the relation between the parallel electric field and current density permits the derivation of the general form Eq. (25) for the inductive solutions. The "lumped resistivity" \mathcal{R}_m appearing in Eq. (27) can be modeled in the manner

described by Fedder et al. (1995) and Raeder (2003), based on adiabatic electron motion in a quasi-static potential drop (Knight, 1973). However, a more realistic parametric model for electron parallel energization is needed. The Knight relation does not properly characterize the apparently nonlinear potential drops that form in downward current channels. The resulting fluxes of upflowing keV-electron beams in such regions should modify the GM solution. The Knight relation also does not capture the physics of superthermal electron energization associated with Alfvén waves in the polar cap boundary region (Chaston et al., 2003). This type of energization may be better modeled by a frequency dependent Ohm's law (e.g. Lysak and Song, 2003), which does not necessarily imply a unipolar current–voltage relation. The field-aligned currents associated with Alfvénic electron acceleration in the auroral-cusp-polar cap boundary region are typically very erratic and dynamic (Nagatsuma et al., 1995). The subgrid physics of Alfvénic acceleration is beyond the current state-of-the-science in global modeling.

Implementation of a simple current–voltage relation forces the question of whether the magnetosphere acts as a constant current source or a constant voltage source (e.g. Paschmann et al., 2003, p. 320). The electrostatic coupling models in prevalent use today assume a constant current source. The statistical patterns of electric and magnetic fluctuations observed above the winter and summer ionospheres suggests that the magnetosphere does in fact act like a current generator, at least in the length-scale regime (3–80 km) on which the study of Vickrey et al. (1986) is based. A complementary study by Weimer et al. (1985) based on DE 1/2 satellite conjunctions rather than seasonal variations suggests that the magnetosphere may act like a voltage generator at transverse scales larger than 100 km. In this case an alternative approach to the one implemented in the LFM and Raeder models may be needed. Instead of treating the magnetic field as known at the low-altitude boundary of the GM model, the electric field and potential at the boundary should be regarded as known. The ionospheric potential is then calculated from Eqs. (16)–(18) with the source term $j_{\parallel i}$ replaced by the $(\Phi_i - \Phi_m)/\mathcal{R}_i$. Nominal values $\mathcal{R}_i \approx 10^9 \Omega\text{-m}^2$ and $\Sigma_p \approx 10 \text{ mho}$ define a length scale $(\Sigma_p \mathcal{R}_i)^{1/2} \approx 100 \text{ km}$ in the resulting elliptic equation for Φ_i . The calculated field-aligned potential drop turns out to be negligible at transverse length scales larger than this MI coupling length, corresponding to the inverted-V scale size (Lyons, 1992).

The scale-dependent resistive response of the MI coupling region to a magnetospheric voltage generator is therefore quite different from that of a magnetospheric current generator. More definitive observations are needed to determine the conditions that favor one type of behavior over the other, and whether the

ability of a magnetospheric dynamo to provide more or less constant current or constant voltage depends on the length and/or time scales of the resulting current system.

Acknowledgements

Bob Lysak provided helpful insights into the low-altitude behavior of Alfvén waves. The research was co-sponsored by the Thayer School of Engineering at Dartmouth College, by the Center for Space Weather Modeling, which is funded by the Science and Technology Centers program of the National Science Foundation under Agreement number ATM-0120950, and by the NASA Sun-Earth Connection Theory program under Grant NAG5-11735.

Appendix A. Dipole geometry

The conventional dipole coordinates (ϕ, v, μ) are defined in terms of spherical polar coordinates (r, θ, ϕ) as $\phi = \phi$, $v = \sin^2 \theta / r$, $\mu = \cos \theta / r^2$. The polar axis is aligned with the dipole axis, so that $\theta = 0$ occurs at the magnetic south pole. The azimuthal angle $\phi = 0$ occurs at 1200 MLT and increases in the eastward direction. The metric scale factors are

$$h_\phi = r \sin \theta, \quad (\text{A.1})$$

$$h_v = \frac{r^2}{\sin \theta (1 + 3 \cos^2 \theta)^{1/2}}, \quad (\text{A.2})$$

$$h_\mu = h_\phi h_v = \frac{M}{B_0}. \quad (\text{A.3})$$

Field lines are labeled by constants values of ϕ and $v = 1/r_L = \text{constant}$, where $r_L = LR_E$ is the geocentric distance to the point, where the field line crosses the magnetic equator ($\theta = \pi/2$).

An alternative coordinate to μ is the distance ℓ along a field line. The point $\ell = \ell_i$ on each fieldline denotes the top of the ionospheric domain, corresponding to the spherical shell $r = r_i$. Along the fieldline, $\sin^2 \theta = R \equiv r/r_L$, and

$$h_\phi = r_L R^{3/2}, \quad (\text{A.4})$$

$$h_v = r_L^2 R^{3/2} (4 - 3R)^{-1/2}, \quad (\text{A.5})$$

$$h_\mu = r_L^3 R^3 (4 - 3R)^{-1/2}. \quad (\text{A.6})$$

A functional relation between ℓ and the radial coordinate r may be derived by integrating

$$d\ell = h_\mu d\mu = -r_L \frac{(1 - 3R/4)^{1/2}}{(1 - R)^{-1/2}} dR. \quad (\text{A.7})$$

to obtain

$$\ell = \frac{r_L}{2\sqrt{3}} \left[x_i(1+x_i^2)^{1/2} - x(1+x^2)^{1/2} + \log \frac{x_i + (1+x_i^2)^{1/2}}{x + (1+x^2)^{1/2}} \right], \quad (\text{A.8})$$

where

$$x = (3 - 3R)^{1/2} \quad \text{and} \quad x_i = (3 - 3R_i)^{1/2} \quad (\text{A.9})$$

and $R_i = r_i/r_L \approx 1/L$. The field line length is $\ell_L = 2\ell(x=0)$. The asymptotic form, valid at mid-to-high latitude and low altitude, is

$$\ell \sim (r - r_i)[1 + (R + R_i)/16] \quad \text{as} \quad R, R_i \rightarrow 0. \quad (\text{A.10})$$

The geometric factors $\alpha_{\phi,v}(\ell)$ in the solution for the electric field are defined as

$$\alpha_{\phi}(\ell) \equiv \int_{\ell_i}^{\ell} \frac{h_{\phi}}{h_v} d\ell' \\ = (2 + R_i)(1 - R_i)^{1/2} - (2 + R)(1 - R)^{1/2} n \quad (\text{A.11})$$

and

$$\alpha_v(\ell) \equiv \int_{\ell_i}^{\ell} \frac{h_v}{h_{\phi}} d\ell' \\ = r_L^2 [(1 - R_i)^{1/2} - (1 - R)^{1/2}], \quad (\text{A.12})$$

with $R(\ell)$ defined implicitly via Eqs. (A.8) and (A.9). Note that $\ell = \ell_i$ occurs at $R = R_i \approx 1/L$.

References

- Allan, W., 1992. Ponderomotive mass transport in the magnetosphere. *Journal of Geophysical Research* 97 (A6), 8483–8493.
- Banks, P.M., Holzer, T.E., 1969. High-latitude plasma transport: the polar wind. *Journal of Geophysical Research* 74 (26), 6317–6332.
- Carlson, C.W., et al., 1998. FAST observations in the downward auroral current region: energetic upgoing electron beams, parallel potential drops and ion heating. *Geophysical Research Letters* 25 (12), 2017–2020.
- Cattell, C., Dombeck, J., Yusof, W., Carlson, C., McFadden, J., 2004. FAST observations of the solar illumination dependence of upflowing electron beams in the auroral zone. *Journal of Geophysical Research* 109 (A02209).
- Chaston, C.C., Bonnell, J.W., Carlson, C.W., McFadden, J.P., Ergun, R.E., Strangeway, R.J., 2003. Properties of small-scale Alfvén waves and accelerated electrons from FAST. *Journal of Geophysical Research* 108 (A4).
- Collin, H.L., Peterson, W.K., Lennartsson, O.W., Drake, J.F., 1998. The seasonal variation of auroral ion beams. *Geophysical Research Letters* 25 (21), 4071–4074.
- Fedder, J.A., Slinker, S.P., Lyon, J.G., Elphinstone, R.D., 1995. Global numerical simulation of the growth phase and the expansion onset for substorm observed by Viking. *Journal of Geophysical Research* 100 (A10), 19083–19093.
- Fridman, M., Lemaire, J., 1980. Relationship between auroral electron fluxes and field-aligned electric potential difference. *Journal of Geophysical Research* 85 (A2), 664–670.
- Keiling, A., Wygant, J.R., Cattell, C.A., Mozer, F.S., Russell, C.T., 2003. The global morphology of wave Poynting flux: powering the aurora. *Science* 299 (5605), 383–386.
- Knight, S., 1973. Parallel electric fields. *Planetary and Space Science* 21 (5), 741–750.
- Knudsen, D.J., Kelley, M.C., Vickrey, J.F., 1992. Alfvén waves in the auroral ionosphere: a numerical model compared with measurements. *Journal of Geophysical Research* 97 (A1), 77–90.
- Lotko, W., 1986. Diffusive acceleration of auroral primaries. *Journal of Geophysical Research* 91 (A1), 191–203.
- Lotko, W., Streltsov, A.V., Carlson, C.W., 1998. Discrete auroral arc, electrostatic shock and suprathermal electrons powered by dispersive, anomalously resistive field line resonance. *Geophysical Research Letters* 25 (24), 4449–4452.
- Lu, G., Reiff, P.H., Burch, J.L., Winningham, J.D., 1991. On the auroral current–voltage relationship. *Journal of Geophysical Research* 96 (A3), 3523–3531.
- Lyon, J.G., Fedder, J.A., Mobarry, C.M., 2004. The Lyon–Fedder–Mobarry (LFM) global MHD magnetospheric simulation code. *Journal of Atmospheric and Solar-Terrestrial Physics*, this issue.
- Lyons, L.R., 1992. Formation of auroral arcs via magnetosphere–ionosphere coupling. *Reviews of Geophysics* 30 (2), 93–112.
- Lyons, L.R., Evans, D.S., Lundin, R., 1979. An observed relation between magnetic field-aligned electric fields and downward electron energy fluxes in the vicinity of the auroral forms. *Journal of Geophysical Research* 84 (A2), 457–461.
- Lyons, L.R., Killeen, T.L., Walterscheid, R.L., 1985. The neutral wind “flywheel” as a source of quiet-time, polar cap currents. *Geophysical Research Letters* 12 (2), 101–104.
- Lysak, R.L., Dum, C.T., 1983. Dynamics of magnetosphere–ionosphere coupling including turbulent transport. *Journal of Geophysical Research* 88 (A1), 365–380.
- Lysak, R.L., Song, Y., 2003. Nonlocal kinetic theory of Alfvén waves on dipolar field lines. *Journal of Geophysical Research* 108 (A8).
- McFadden, J.P., et al., 1998. Spatial structure and gradients of ion beams observed by FAST. *Geophysical Research Letters* 25 (12), 2021–2024.
- Moore, T.E., Lundin, R., Alcayde, D., André, M., Ganguli, S.B., Temerin, M., Yau, A., 1999. Source processes in the high-latitude ionosphere. In: Hultqvist, B., Øierset, M., Paschmann, G., Treumann, R. (Eds.), *Magnetospheric Plasma Sources and Losses*. Kluwer Academic Publishers, Dordrecht, The Netherlands, pp. 7–84.
- Nagatsuma, T., Fukunishi, H., Mukai, T., 1995. Spatial relationships between field-aligned currents and suprathermal electron beams observed at the poleward boundary of the nightside auroral oval. *Journal of Geophysical Research* 100 (A2), 1625–1637.
- Nagatsuma, T., Fukunishi, H., Hayakawa, H., Mukai, T., Matsuoka, A., 1996. Field-aligned currents associated with Alfvén waves in the poleward boundary region of the

- nightside auroral oval. *Journal of Geophysical Research* 101 (A10), 21715–21729.
- Paschmann, G., Haaland, S., Treumann, R. (Eds.), 2003. *Auroral Plasma Physics*, vol. 15. Space Sciences Series of ISSI, Kluwer Academic Publishers, Dordrecht, The Netherlands.
- Persoon, A.M., Gurnett, D.A., Peterson, W.K., Waite Jr., J.H., Burch, J.L., Green, J.L., 1988. Electron density depletions in the nightside auroral zone. *Journal of Geophysical Research* 93 (A3), 1871–1895.
- Pokhotelov, D., Lotko, W., Streltsov, A.V., 2002. Effects of the seasonal asymmetry in ionospheric Pedersen conductance on the appearance of discrete aurora. *Geophysical Research Letters* 29 (10).
- Proehl, J.A., Lotko, W., Kouznetsov, I., Geimer, S.D., 2002. Ultralow-frequency magnetohydrodynamics in boundary-constrained geomagnetic flux coordinates. *Journal of Geophysical Research* 107 (A9).
- Raeder, J., 2003. Global geospace modeling: tutorial and review. In: Büchner, J., Dum, C.T., Scholer, M. (Eds.), *Space Plasma Simulation*, vol. 615. Lecture Notes in Physics, Springer, Berlin.
- Raeder, J., Wang, Y., Fuller-Rowell, T., 2001. Geomagnetic storm simulation with a coupled magnetosphere–ionosphere–thermosphere model. In: Song, P., Siscoe, G., Singer, H.J. (Eds.), *Space Weather*, vol. 125, Geophysical Monograph, American Geophysical Union, Washington DC, p. 377.
- Rankin, R., Fenrich, F., Tikhonchuk, V., 2000. Shear Alfvén waves on stretched magnetic field lines near midnight in Earth's magnetosphere. *Geophysical Research Letters* 27 (20), 3265–3268.
- Ridley, A.J., Richmond, A.D., Gombosi, T.I., Zeeuw, D.L.D., Clauer, C.R., 2003. Ionospheric control of the magnetospheric configuration: thermospheric neutral winds. *Journal of Geophysical Research* 108 (A8).
- Rönmark, K., 2002. Auroral current–voltage relation. *Journal of Geophysical Research* 107 (A12).
- Schunk, R. W., Nagy, A. F., 2000. *Ionospheres: Physics, Plasma Physics, and Chemistry*. Cambridge Atmospheric and Space Science Series, Cambridge University Press, New York.
- Streltsov, A.V., Lotko, W., 2003. Absorption and reflection of Alfvénic power in the low-altitude magnetosphere. *Journal of Geophysical Research* 108 (A4).
- Temerin, M., Carlson, C.W., 1998. Current–voltage relationship in the downward auroral current region. *Geophysical Research Letters* 25 (13), 2365–2368.
- Tung, Y.-K., Carlson, C.W., McFadden, J.P., Klumpar, D.M., Parks, G.K., Peria, W.J., Liou, K., 2001. Auroral polar cap boundary ion outflow observed on FAST. *Journal of Geophysical Research* 106 (A3), 3603–3614.
- Vasyliunas, V.M., 1970. Mathematical models of magnetospheric convection and its coupling to the ionosphere. In: McCormac, B.M. (Ed.), *Particles and Fields in the Magnetosphere*. D. Reidel Publ. Co, Dordrecht, The Netherlands, pp. 60–71.
- Vickrey, J.F., Livingston, R.C., Walker, N.B., Potemra, T.A., Heelis, R.A., Kelley, M.C., Rich, F.J., 1986. On the current–voltage relationship of the magnetospheric generator at intermediate spatial scales. *Geophysical Research Letters* 13 (6), 495–498.
- Vogt, J., Haerendel, G., 1998. Reflection and transmission of Alfvén waves at the auroral acceleration region. *Geophysical Research Letters* 25 (3), 277–280.
- Wang, W., Wiltberger, M., Burns, A.G., Solomon, S., Killeen, T.L., Maruyama, N., Lyon, J.G., 2004. Initial results from the coupled magnetosphere–ionosphere–thermosphere model: Thermosphere–ionosphere responses. *Journal of Atmospheric and Solar-Terrestrial Physics*, this issue.
- Weimer, D.R., Goertz, C.K., Gurnett, D.A., Maynard, N.C., Burch, J.L., 1985. Auroral zone electric fields from DE 1 and 2 at magnetic conjunctions. *Journal of Geophysical Research* 90 (A8), 7479–7494.
- Wiltberger, M., Wang, W., Burns, A., Solomon, S., Lyon, J.G., Goodrich, C.C., 2003. Results from the Lyon–Fedder–Mobarry global magnetospheric model for the electrojet challenge. *Journal of Atmospheric and Solar-Terrestrial Physics* 65 (11–13), 1213–1222.
- Wiltberger, M., Wang, W., Burns, A., Solomon, S., Lyon, J.G., Goodrich, C.C., 2004. Initial results from the coupled magnetosphere–ionosphere–thermosphere model: magnetospheric and ionospheric responses. *Journal of Atmospheric and Solar-Terrestrial Physics*, this issue.
- Wolf, R.A., 1973. The Quasistatic (Slow-Flow) Region of the Magnetosphere. D. Reidel Publ. Co., Dordrecht, The Netherlands, pp. 303–368.
- Yau, A.W., Walen, B.A., Peterson, W.K., Shelley, E.G., 1984. Distribution of upflowing ionospheric ions in the high-altitude polar cap and auroral ionosphere. *Journal of Geophysical Research* 89 (A7), 5507–5522.
- Yoshikawa, A., 2002. Excitation of the hall-current generator by field-aligned current closure, via an ionospheric divergent hall current during the transient phase of magnetosphere–ionosphere coupling. *Journal of Geophysical Research* 107 (A12).